

# Chirality induced topological nature of electrons in DNA-like materials

Yizhou Liu\*, Jiewen Xiao\*, Jahyun Koo, Binghai Yan<sup>†</sup>

Department of Condensed Matter Physics, Weizmann Institute of Science, Rehovot 76100, Israel

March 31, 2022

**Topological aspects of DNA and similar chiral molecules are commonly discussed in geometry, while their electronic structure's topology is less explored. Recent experiments revealed that DNA could efficiently filter spin-polarized electrons, called the chiral-induced spin-selectivity (CISS). However, the underlying correlation between chiral structure and electronic spin remains elusive. In this work, we reveal an orbital texture in the band structure, a topological characteristic induced by the chirality. We find that the orbital texture enables the chiral molecule to polarize the quantum orbital, called the orbital polarization effect (OPE). The OPE induces spin polarization assisted by the spin-orbit interaction only from the metal contact and also leads to magnetism-dependent conductance and chiral separation. Beyond CISS, we predict that OPE can also induce spin-selective phenomena even in achiral but inversion-breaking materials.**

## Introduction

In chemistry and biochemistry, the chirality is the geometric asymmetry of a large group of molecules with a nonsuperposable mirror image, either left- or right-handed. It plays a prominent role in chemistry and biology (*1*) for example in the enantioselective catalysis (*2*) and drug design (*3*). In physics, the chirality usually refers to the locking of spin and motion such as the Weyl fermions (*4*) and neutrinos (*5*). Although the chirality represents seemingly irrelevant characters in different fields, recent experiments (*6*) reveal an unexpected correlation between the chiral geometry and the electronic spin. When they transmitted through DNA, electrons get highly spin-polarized, and the polarization depends on the chirality. This effect is called chiral-induced spin selectivity (CISS)(see Refs. (*7, 8*) for review) and is also observed in many other chiral molecules (*9, 10, 11, 12, 13, 14, 15, 16*) and even some chiral crystals (*17, 18, 19*). The high spin polarization is induced and manipulated in ways not previously imagined (*20*).

In the last decade, the CISS effect has demonstrated appealing application potential in spintronic devices (21, 22, 12, 23, 13, 14, 15, 24, 25, 26, 27, 28, 29, 30, 31), chiral electrocatalysis (32, 33, 34, 35, 36) and enantiomer selectivity (37, 38). For instance, chiral molecules were found to adsorb on a ferromagnetic substrate with different speeds that depend on both the chirality and the substrate magnetization, leading to efficient separation of enantiomers (37). When contacting to magnetic leads, the chiral molecule exhibits magnetization-dependent resistivity, i.e. the magnetoresistance (MR) (21, 12, 23, 24, 26, 27, 39, 40). However, the physical origin of CISS, i.e. the relation between the chiral structure and the electron spin, is still debated.

The first characteristic feature of CISS experiments is their robustness at room temperature (Ref. (8) and references therein). The second feature is that they are dynamical phenomena that usually involve electron tunneling or electron transfer in the non-equilibrium process. Chiral molecules like DNA exhibit no spin polarization at the ground state, and the CISS effect vanishes at equilibrium. For example, the chiral separation disappears after the substrate and molecules reach thermodynamic equilibrium after a long enough time (37, 38). Another feature that usually attracts little attention is that chiral molecules commonly have direct contact with a noble metal (e.g., gold) substrate, thin-film, or nanoparticles in these experiments.

Although many theories have been developed to understand the CISS effect (41, 42, 43, 44, 45, 46, 47, 48, 49, 50, 51, 52, 53, 54, 55, 56, 57, 58, 59, 60, 61, 62, 63, 64, 65, 66, 67, 68, 69), the consensus is not reached. Most models consider the chiral molecule as a spin filter and require an effective spin-orbit coupling (SOC) in the molecule to couple the electron motion and spin. However, it is known that the experimentally measured SOC is no larger than a few meV in related organic systems (e.g. the curved carbon nanotubes (70, 71)). Thus it is challenging to rationalize the robustness of CISS at room temperature (26 meV), even though several scenarios were proposed to enhance the spin polarization. In addition, there are debates on the role of dephasing in CISS (42, 43, 45, 46, 48, 50, 55).

The chiral electronic structure of Weyl semimetals (72, 73, and references therein) inspires us to explore the band structure topology of DNA and similar chiral molecules. In this work, we reveal an ubiquitous topological orbital texture in the chiral lattice and propose a mechanism that the chiral molecule acts as an orbital polarizer or an orbital filter, rather than a spin filter, in the CISS effect. The orbital polarization effect (OPE) does not require SOC from the molecule and remains much robust against the temperature fluctuation. The orbital refers to the atomic orbital angular momentum (OAM) of the wave function. By calculations with the Landauer-Büttiker formalism, we demonstrate that electrons get orbital-polarized after transmitting through the chiral molecule, in which the polarization depends on the chirality. (i) When electrons propagate from the lead through the molecule, the chirality filters the orbital and subsequently selects the spin, because orbital and spin are pre-locked by SOC in the heavy-metal lead. Thus, these transmitted electrons become spin-polarized, leading to the CISS, as illustrated in **Figure 1c**. (ii) When electrons transmit from the chiral molecule into the lead, the orbital-polarization induces spin polarization also because of SOC in the lead. (iii) Furthermore, when it is magnetic (spin-polarized), the lead is also orbital-polarized because of SOC. If the orbital polarization of the lead matches that of the molecule, the electron tunneling is fast and otherwise slow, leading to

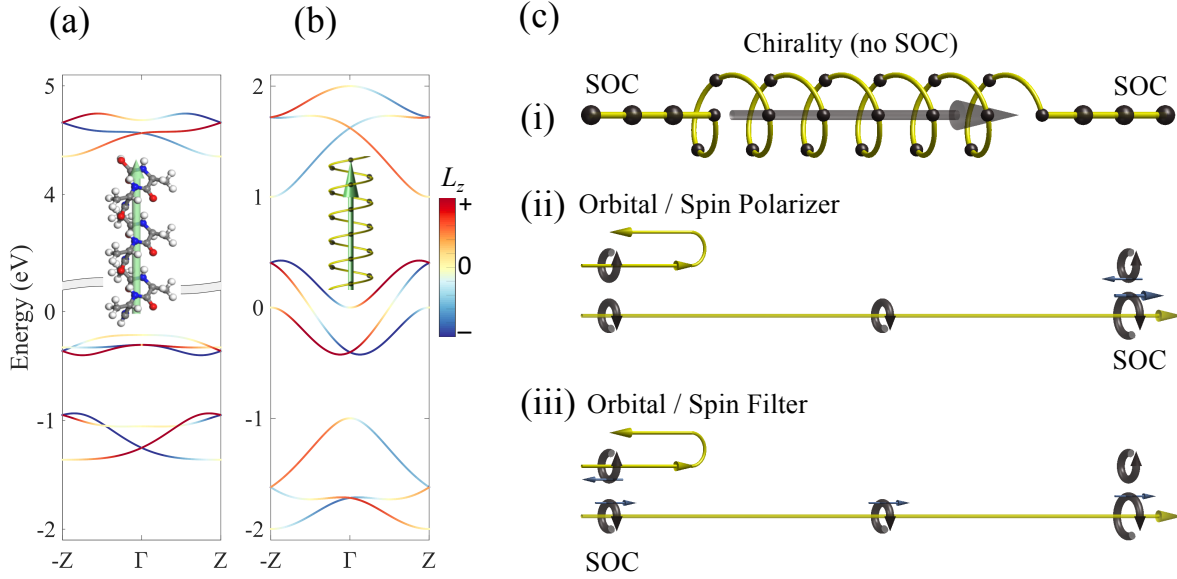


Figure 1: **The orbital polarization and the orbital texture.** (a) The *ab initio* band structure of the right-handed peptide  $3_{10}$  helix with orbital texture. The orbital texture refers to the parallel or anti-parallel relation between orbital polarization  $L_z$  and the momentum. The inset shows the atomic structure the  $3_{10}$  helix where gray, blue, red, and white spheres represent C, N, O, and H atoms. (b) The band structure of a tight-binding model of the helix. The helix has a three-fold screw rotation (see inset), same as the  $3_{10}$  helix. (c) Illustration of the orbital polarization effect in transport. (i) The helix (small black spheres) connects two leads that are linear atomic chain (large black spheres). The spin-orbit coupling (SOC) exists only in leads but not in the chiral helix. At given energy, the orbital gets polarized to  $+L_z$  as the electron transmits through the chiral molecule. (ii) When electrons run into the right lead where SOC exists, the orbital polarization induces spin polarization. The half circles with arrows represent the  $\pm L_z$  orbital. Thin arrows represent the spin. The larger orbital and spin stand for the orbital and spin polarization, respectively, are in the right lead. (iii) The chiral molecule filters the  $+L_z$  state but suppresses the  $-L_z$  state injected from the left lead. The yellow curves illustrate the scattering trajectory with arrows. If the spin is pre-locked to the orbital in the left lead, transmitted electrons become spin-polarized due to the orbital filtering. We note that the multiple-mode leads allow the emergence of spin polarization in the two-terminal conductance despite the presence of the time-reversal symmetry.

MR. It also induces different adsorbance / desorbance speed of molecules with opposite chirality, resulting in the chirality separation on the magnetic substrate (37). We rationalize the CISS and related phenomena without requiring the presence of SOC in the molecule. We point out that the heavy metal lead plays the role of a spin-orbit translator that converts the orbital polarization into the spin polarization. Additionally, we also clarify the debates about dephasing. Furthermore, our work reveals the deep connection between CISS and the magnetochiral anisotropy (74) discussed in the condensed-matter physics community. Besides chiral molecules, we predict that OPE can also lead to spin-selective effects in achiral but noncentrosymmetric molecules and solids.

## Results

### Topological Orbital Texture

The band structure of the chiral lattice exhibits a topological feature that we call the orbital texture. We take a periodic chain of the right-handed peptide  $3_{10}$  helix as an example. It is a typical secondary structure found in proteins and polypeptides, which was also studied in the CISS experiment (75). The helix exhibits the three-fold screw rotation around the  $z$ -axis. This symmetry induces the Dirac-like band crossings at the zone center ( $\Gamma$ ) and boundary ( $\pm Z$ ), as shown in the *ab initio* band structure in **Figure 1a**. It always sticks three bands together as a general consequence of the nonsymmorphic symmetry in the band structure topology (76, 77). Thus, the nature of a chiral band structure involves multiple bands, beyond the one-band description. Here, SOC is ignored in the band structure since it is negligibly small.

A salient feature in the band structure is the orbital polarization  $L_z$ . The  $L_z$  refers to the atomic OAM. Without loss of generality, the OAM operator  $\hat{L}_z$  in the  $p_{x,y,z}$  basis, is known

to be,  $\hat{L}_z = \begin{bmatrix} 0 & -i & 0 \\ i & 0 & 0 \\ 0 & 0 & 0 \end{bmatrix}$ , where we omit the index for atomic sites. It has three eigen states

$p_{\pm} \equiv (p_x \pm ip_y)/\sqrt{2}, p_z$  with  $L_z = \pm 1, 0$ , respectively. Because of the inversion symmetry (IS)-breaking, the Bloch wave function is allowed to exhibit nonzero OAM at the finite momentum. The screw rotation constrains that the OAM aligns along the  $z$  direction, i.e.  $L_z$ . It is worth stressing that the OAM represents the self-rotation of the wave functions around atomic centers and is not a conserved quantity. To respect the time-reversals symmetry (TRS),  $L_z$  exhibits opposite signs at the  $k_z$  and  $-k_z$  points, as shown in **Figure 1a**. Similar to the chirality of a Weyl fermions (72, 73),  $L_z$  and  $k_z$  are always parallel or anti-parallel, which depends on the molecule chirality. Different from the Weyl point that exhibits infinitely large polarization, the  $L_z$  vanishes to zero at  $\Gamma$  and  $\pm Z$  because of TRS. According to the symmetry analysis, we point out that such an orbital texture is ubiquitous for a chiral lattice with and without a helix structure. Even when the screw rotational symmetry vanishes in a non-helical structure, the orbital texture still preserves because of the IS-breaking.

We adopt a right-handed helix model to represent a chiral chain. The helix includes three

sites in the primitive unit-cell and exhibits the same three-fold screw rotation as the  $3_{10}$  helix. We set three  $p$ -orbitals ( $p_{x,y,z}$ ) on each site and consider the nearest neighboring hopping in a tight-binding model (see more details in SM). As shown in **Figure 1b**, its band structure also exhibits the same band degeneracy and orbital texture. For a linear chain, in contrast, the orbital polarization is strictly zero at all  $k$ -points because of the presence of both inversion symmetry and TRS.

The topological orbital texture originates in the anisotropic hopping of the chiral orbital along the chiral chain. For generality, we consider a right-hand helical chain with the  $n$ -fold screw rotation, in which the site  $i$  has two nearest neighbors,  $i + 1$  along  $+z$  and  $i - 1$  along  $-z$ . We set two bases,  $p_{\pm}$ , at each site, and set the hopping integral as the simple Slater-Koster type (78). Among the same orbital ( $p_+$  or  $p_-$ ), the hoppings from  $i$  to  $i \pm 1$  are the same. From  $p_+$  to  $p_-$ , however, the hopping from  $i$  to  $i + 1$  is different from that from  $i$  to  $i - 1$  by a phase factor  $e^{-i4\pi/n}$ . If the chirality reverses, the phase  $-4\pi/n$  also changes its sign. Take a helix with  $n = 4$ , for example. The inter-orbital hopping is different by a “-” sign between the up and down directions. It means that  $p_+$  prefers a certain direction in hopping, while  $p_-$  prefers the opposite direction. Consequently, the anisotropic inter-orbital hopping induces the orbital texture in the band structure. It also indicates that the orbital texture is as robust as the hopping integral’s energy scale, i.e., the bandwidth. At a finite Fermi energy in the band structure, oppositely propagating electrons carry opposite orbital polarization, resulting in the orbital polarization effect discussed in the following.

## Two-terminal Transport and Dephasing

In previous theoretical studies (42, 43, 44, 48, 50, 52, 53, 55, 58, 60, 62), the dynamic CISS process is usually mapped to a transmission problem between two achiral leads through a chiral molecule that exhibits effective SOC due to different mechanisms. The spin polarization of the transmitted electrons is evaluated as evidence of the CISS. In this work, we adopt the same transmission model but remove SOC from the chiral molecule. As illustrated in **Figure 2a**, we add a linear part with atomic SOC between the chiral molecule and both leads, to simulate the fact that chiral molecules commonly contact to the noble metal substrate. Both leads and the chiral molecule have no SOC. Achiral linear chains represent leads and the SOC part. The tight-binding Hamiltonian of the whole system (both leads and the center region) is constructed with atomic  $p$ -orbitals ( $p_x, p_y, p_z$ ) and the hopping parameters in the same way as that for the band structure calculation in **Figure 1c**.

We obtain the scattering matrix  $S_{nm}$  from the left ( $L$ ) to the right ( $R$ ) lead by the scattering theory and obtain the conductance by the Landauer-Büttiker formula (79),

$$G_{L \rightarrow R} = \frac{e^2}{h} \sum_{n \in R, m \in L} |S_{nm}|^2, \quad (1)$$

where  $S_{nm}$  is the transmission amplitude from  $m$ -th eigenstate in the left lead to the  $n$ -th

eigenstate in the right lead. In the following discussion, we will use  $G$  for  $G_{L \rightarrow R}$  if it is not noted specifically.

In both leads, the spin ( $S_z = \uparrow\downarrow$ ) and the orbital ( $L_z = \pm, 0$ ) are conserved quantities because of the disappearance of SOC and the axial rotational symmetry, respectively. Thus, one can classify the conductance into each  $S_z$  or  $L_z$  channels. Given the non-polarized injection state from the left lead, we estimate the spin and orbital, respectively, polarized conductance of transmitted electrons in the right lead by,

$$G_{S_z} = G_{L \rightarrow R \uparrow} - G_{L \rightarrow R \downarrow} \quad (2)$$

$$G_{L_z} = G_{L \rightarrow R +} - G_{L \rightarrow R -}, \quad (3)$$

where  $G_{L \rightarrow R S_z(L_z)}$  represents the conductance from the  $L$  lead to the  $S_z(L_z)$  channel of the  $R$  lead. Here,  $G_{L \rightarrow R L_z=0}$  is omitted because the  $L_z = 0$  state does not contribute to the total polarization. Corresponding spin and orbital polarization ratios are  $P_{S_z} = G_{S_z}/G$  and  $P_{L_z} = G_{L_z}/G$ , respectively.

To demonstrate the CISS, we will show that electrons go through the chiral molecule and get spin-polarized, which is caused by the orbital polarization effect, by calculating  $G_{S_z}$  and  $G_{L_z}$ . We have performed all conductance calculations by our program and verified them with the quantum transport package Kwant (80). Related model parameters can be found in the SM.

The dephasing related to the inelastic process was frequently discussed as a necessary condition (42, 43, 50, 60) to generate CISS. The single-mode leads employed in these models prohibit the spin current in the presence of TRS (81, 82, 54). The existence of multiple modes in our leads allows the emergence of spin current without introducing the extra dephasing. We note that multiple modes represent the more realistic condition of the transition metal contact, compared to the single-mode model. However, the existence of the two-terminal MR, i.e.  $G_{L \rightarrow R(+M)} \neq G_{L \rightarrow R(-M)}$ , requires the dephasing to leak electrons into virtual leads (83). Otherwise, the charge conservation forces the reciprocity regardless of the mode number in leads. Therefore, the role of dephasing in CISS depends on whether the lead is magnetic or not, as discussed in the following sections. In calculations, we introduce the dephasing parameter  $i\eta$  as the Büttiker virtual probe (83) equally to each site of the chiral molecule. As long as the dephasing exists, we find that the nonreciprocal MR manifests the CISS effect in a two-terminal device.

## Orbital Polarization Effect and CISS

The orbital texture induces the OPE as electrons go through the chiral molecule. Different from the band structure, the energy level of a finite-size molecule exhibits no dispersion. Nevertheless, we can still use insights from the band structure and regard the molecule wave function as the superposition of the right and left movers from the band structure. Since right and left movers exhibit opposite  $L_z$ , the molecule displays no orbital polarization at the ground state. When an electron tunnels through the molecule from left to right, it transmits through the right mover channel, as illustrated in **Figure 1c**.

The chiral molecule plays roles as both an orbital filter and an orbital polarizer. If we approximate  $L_z$  as conserved, then  $L_z$  does not flip as traveling through the molecule. We can regard the chiral channel as an orbital filter that only allows a given  $L_z$  to pass, as illustrated in **Figure 1c**. The orbital filter is essential at the interface between the chiral molecule and the left lead, where the incident orbitals get filtered. However,  $L_z$  is not a conserved quantity in the molecule and will flip in the transmission. The  $G_{L_z}$  also includes substantial orbital-flip contribution due to the transmission from  $p_-$  and  $p_z$  states at left lead to  $p_+$  at right (see the channel-specific conductance in SM), caused by the orbital polarizer effect. It is interesting to see that the chiral channel can even polarize the  $|L_z = 0\rangle$  state. The orbital polarizer is vital when electrons run from the molecule into the right lead. These emitting electrons can induce intense orbital polarization in the right lead.

The chiral molecule exhibits preferred transmission for electrons with the orbital polarization parallel or anti-parallel, which is determined by the chirality to the transmitting direction at a specific energy. Our conductance calculations confirm the OPE, as indicated by the nonzero  $G_{L_z}$  in **Figure 2b**. We turn off the SOC in the whole device and observe no spin polarization in the conductance since the motion and spin separate at all. We recall that the linear chain exhibits no orbital texture. The OPE is only due to the orbital texture in the chiral region.

With SOC from the contact, OPE eventually leads to the spin polarization. We turn on the atomic SOC ( $\lambda_{SOC}$ ) in the short linear chains. For simplicity, we put the SOC part attached to both leads to make them symmetric. As shown in **Figure 2**, the spin polarization ( $P_{S_z}$ ) increases as  $\lambda_{SOC}$  increases. At given  $\lambda_{SOC}$ , one can find that  $G_{S_z}$  is roughly proportional to  $G_{L_z}$ . Here, the SOC converts the orbital polarization to the spin polarization, since SOC locks the spin and orbital together. For example,  $p_+$  ( $p_-$ ) is locked to the  $\uparrow$  ( $\downarrow$ ) spin in  $|j_m = \frac{3}{2}\rangle$  ( $|j_m = -\frac{3}{2}\rangle$ ) state ( $j_m$  is the  $z$  projection of the total angular momentum). Although  $|j_m = \pm\frac{3}{2}\rangle$  are degenerate in the SOC regime, the chiral molecule filters the  $p_+$  ( $p_-$ ) state and consequently selects the  $\uparrow$  ( $\downarrow$ ) spin around the energy  $-1.8$  ( $+1.8$ ) eV in **Figure 2d**. If reversing the chirality of the molecule, the orbital texture gets inverted, and thus, the spin polarization can be flipped.

As increasing the atomic number ( $N$ ) in the chiral chain, the calculated  $P_{S_z}$  first increases and soon gets nearly saturated after  $N = 7$ . In reality, the critical length depends on the material details. The region of increasing  $P_{S_z}$  can interpret the length-enhanced spin polarization in the experiment (6, 12, 84). We note that  $N = 1, 2$  are actually achiral segments and thus corresponding  $P_{S_z}$  is zero. The OPE is a robust effect compared to the temperature because the orbital texture is in the order of magnitude of the bandwidth (e.g.  $\sim 0.5$  eV for the  $3_{10}$  helix in Figure 1a) and thus is much larger than the room temperature. Given than SOC in the heavy metal lead lies in a similar magnitude, the resultant spin polarization in CISS becomes a strong phenomenon in the ambient condition.

The existence of spin polarization does not require extra dephasing in our calculations. This is because we have three modes in each lead. We find that the spin conductance  $G_{S_z}$  is insensitive to the moderate dephasing with strong SOC and turns to decrease when the large dephasing violates the coherence (see Figure 2c and SM). If single-mode leads are employed, we verify  $G_{S_z} = 0$  without dephasing (see SM).

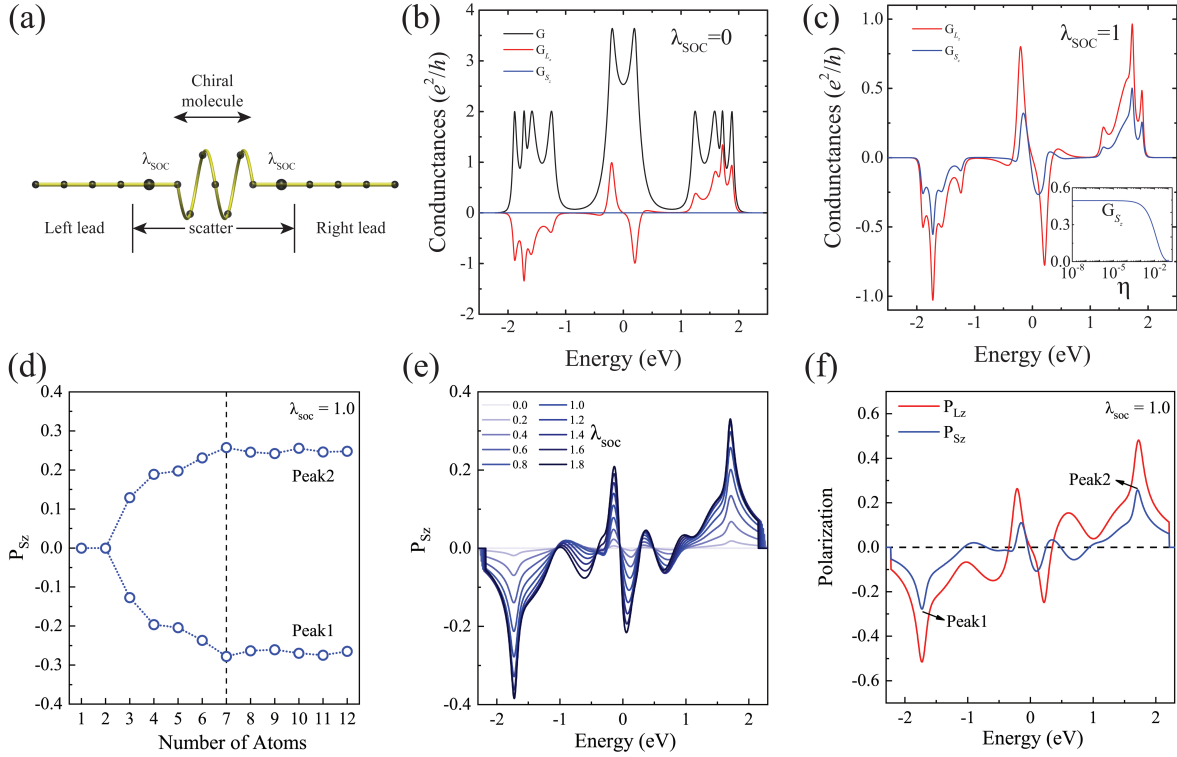


**Figure 2: Orbital polarization and spin polarization in the conductance.** (a) The transport model includes two linear leads and the chiral molecule with two helical units long. The SOC is only added to the intermediate site between the chiral molecule and the lead. (b) The orbital polarization  $G_{L_z}$  exists while the spin conductance  $G_{S_z} = 0$  for  $\lambda_{SOC} = 0$ .  $G$  is the total conductance. (c)(e)&(f)  $G_{S_z}$  and the spin polarization rate  $P_{S_z}$  increases as turning on SOC. The  $G_{S_z}$  (peak value around 1.8 eV) dependence on the dephasing term  $\eta$  is shown in the inset of (c). (d) Peaks of  $P_{S_z}$  [noted in (c)] increase quickly as increasing the length of the chiral molecule and get almost saturated after the number of atoms is 7 [the same length as the model shown in (a)]. No dephasing is included in calculations except the inset of (c).

As discussed above, the required SOC comes from heavy metal leads such as gold (sometimes by contacts with the In-doped SnO<sub>2</sub> (33), GaN, and CdSe (15) in experiments). The  $\lambda_{SOC}$  dependence of CISS can be examined in transport experiments to verify our OPE theory. However, photoemission experiments of CISS deserve subtle treatment since they do not involve two-terminal devices. In intense light irradiation, the substrate ejects electrons into the vacuum through a layer of chiral molecules, and then the magnetization of photoelectrons is measured by a Mott polarimeter (11, 14). We note that the Mott detector is sensitive to both the orbital moment and spin moment. Since the orbital moment does not rely on any SOC, the detected total magnetization of photoelectrons may be less sensitive to the substrate SOC, compared to the transport measurement.

## Magnetoconductance and Magnetic Chiral Separation

The orbital polarization can also rationalize these experiments on the MR (21, 22, 12, 23, 13, 14, 24, 26, 27) and chiral separation by the magnetic substrate. (37, 38). In MR experiments, a gold nanoparticle was included between one lead and the chiral molecule and the other lead is magnetic such as nickel. Switching the lead magnetization induces the change of resistance. For the chirality selection, the substrate is a ferromagnetic Co film covered by a thin layer (several nanometers) of gold. Molecules with opposite chirality get adsorbed to the substrate at a different speed, leading to the separation of chiral enantiomers. In the transient state when the molecule gets adsorbed on a metal surface, a small amount of charge transfer occurs between them (75). The speed of the charge transfer, which is a quantity similar to the conductance, characterizes the speed of the adsorbance. Therefore, we can gain useful insights both for the adsorbance and MR from the conductance calculations.

As injecting spin-polarized electrons from the substrate, the gold regime becomes spin-polarized and also orbital polarized because of SOC. Then the orbital direction is locked with the magnetization direction. If this orbital matches the following OPE in the chiral molecule, the total conductance is large and otherwise small. As a consequence, different chirality and magnetization can lead to different MR and speed of adsorbance as well.

We employ the same two-terminal model and add an exchange field ( $M$ ) along the  $z$ -direction to the spin components in both leads. The intermediate SOC regime mimics the noble metal part. As shown in **Figure 3b**, the conductance changes as switching the sign of magnetization. The change of conductance  $\Delta G$  is proportional to the magnitude of  $M$ . One can understand the role of the OPE by observing  $G_{S_z}$  and  $G_{L_z}$ , as shown in **Figure 3d**. When flipping the magnetization, it is not surprising  $G_{S_z}$  changes its sign at a certain energy. Subsequently, the magnitude of  $G_{L_z}$  varies because of the SOC. In Figure 3d, the increase (decrease) of  $|G_{L_z}|$  around 1.8 (-1.8) eV rationalizes the increase (decrease) of  $G$  at the same energy regime in Figure 3b, as a consequence of the OPE. Here, we include a finite dephasing parameter.

As shown in **Figure 3c**,  $\Delta G = 0$  if  $\eta = 0$ . As increasing  $\eta$ ,  $\Delta G$  first increases quickly and then reduces if  $\eta$  is too large (see more in SM). In the coherent two-terminal measurement ( $\eta = 0$ ) (85), the reciprocity theorem requires  $G_{L \rightarrow R}(M) = G_{L \rightarrow R}(-M)$ . However, the virtual

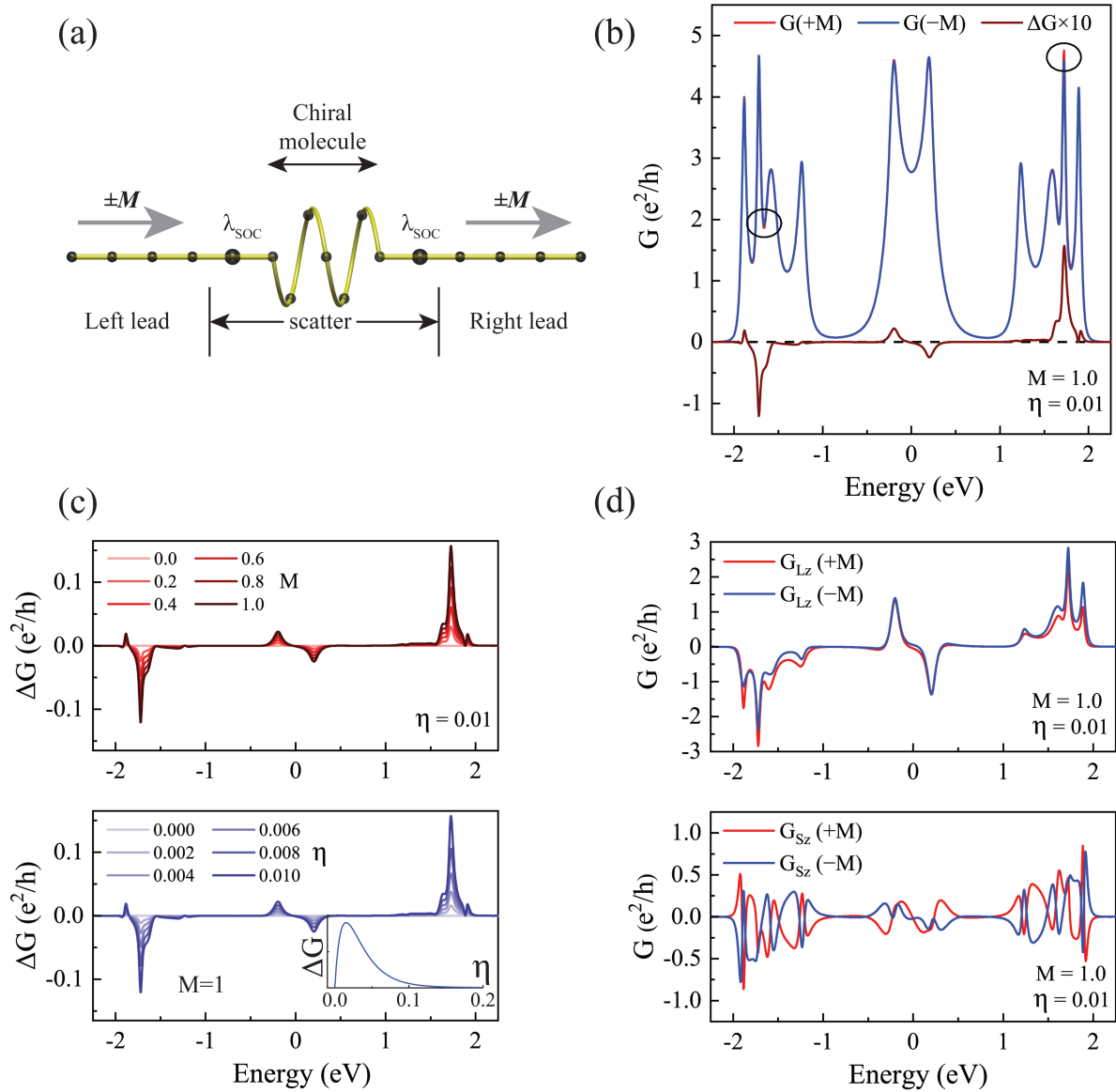


Figure 3: **Magnetoresistance with magnetic leads.** (a) The device model with two magnetized ( $\pm M$ ) leads. (b) The total conductance varies when flipping the lead magnetization. (c) The change of the conductance  $\Delta G = G(+M) - G(-M)$  increases as increasing the magnitude of  $M$  and the dephasing term  $\eta$ . The inset of the lower panel shows the dependence of  $\Delta G$  (the right peak at about 1.8 eV on  $\eta$  in a larger scale). (d) As flipping  $M$  from  $-$  to  $+$ ,  $G_{S_z}$  changes sign in the general energy window, leading to changes of  $G_{L_z}$ . The increase (decrease) of  $G_{L_z}$  accounts for the increase (decrease) of  $G$  in (b), as an inverse effect of the orbital polarization. We set  $\lambda_{\text{SOC}} = 0.5$  in all these calculations.

lead ( $i\eta$ ) releases this constrain, resulting in nonzero MR. The nonreciprocal MR is well consist with the fact that the differential conductance ( $dI/dV$ ) changes as reversing  $M$  in experiment.

It should be noted that the dephasing is actually zero if no current flows in the device. If the dephasing is too large, electrons are completely incoherent and feel no OPE in the transport. This explains the decreasing of MR for large dephasing. In addition, we verify that calculated conductance satisfies the *global* Onsager's reciprocal relation,  $G_{L \rightarrow R}(M) = G_{R \rightarrow L}(-M)$  (see SM).

The unidirectional conductance can also rationalize the chiral separation. We note that the adsorbance and desorbance correspond to opposite charge transfer directions between the substrate and the chiral molecule. Therefore, a chiral molecule releases slower (faster) from the surface if it adsorbs faster (slower). Both adsorbance and desorbance guarantees that a substrate with certain magnetization attracts one chirality faster than the opposite chirality.

## Discussion

### Unidirectional Conductance and Electric Magneto-chiral Anisotropy

In the CISS-induced MR, as discussed above, the lead magnetization and the chirality together pick up one direction, along which the current flow is favored in the device. The conductance ( $G$ ) and resistance ( $R$ ) can be describe to the leading order as,

$$G(\mathbf{M}, \mathbf{I}) = G^0 + G^\chi \mathbf{M} \cdot \mathbf{I} \quad (4)$$

$$R(\mathbf{M}, \mathbf{I}) = R^0 - R^\chi \mathbf{M} \cdot \mathbf{I} \quad (5)$$

where  $R^0 = 1/G^0$ ,  $R^\chi = G^\chi/(G^0)^2$ ,  $\mathbf{M}$  stands for the magnetization in the lead,  $\mathbf{I}$  for the current,  $G^\chi$  for the chirality ( $\chi$ ) determined conductance ( $G^\chi = -G^{-\chi}$ ).  $G^0$  is the ordinary conductivity while  $G^{(2)}$  characterizes the unidirectional contribution. We point out that the linear relation of  $G$  on  $I$  comes from the approximate linear dependence on dephasing in the small  $\eta$  region. So the specific form of Eqs. 4 & 5 can be modified by the dephasing dependence. For the I-V relation, we obtain

$$I = G^0 V / (1 - G^\chi M V) \approx G^0 V + G^0 G^\chi M V^2 + \mathcal{O}(V^3) \quad (6)$$

where the sign of  $\mathbf{M}$  can be  $\pm$ . Equation 6 agrees with the nonlinear I-V curves in experiments (21, 12, 23, 24, 26, 27, 84). It indicates that the CISS-induced MR can be probed by two-terminal experiments, to be accurate, in the nonlinear regime, which was debated recently (60, 86, 62, 87). However, one can gain significant insights into MR by the linear-response scenario by assuming a dephasing term, reminding that the dephasing commonly exists due to the energy dissipation and inelastic effects at finite current. The anisotropic conductance can lead to the current rectification. Suppose applying an ac electric field  $E(t) = E_0 \cos \omega t$  between two leads, the  $V^2$  term in Eq. 6 leads to a dc current density averaged in the driving period. The dc current (or open-circle

voltage) may be considered for photon-detection or energy-harvesting from the long-wavelength light without requiring specific polarization in light.

The nonreciprocal conductance described by Eqs. 4 & 5 reminisces the electrical magnetochiral anisotropy (EMChA) discussed in literature (74, 88), which was observed in chiral conductors (e.g., bismuth helix (74)) in the presence of a magnetic field. Corresponding resistance change ( $\Delta R$ ) of a chiral conductor (chirality  $\chi = \pm 1$ ) subject to a longitudinal magnetic field  $\mathbf{B}$  is expressed as  $\Delta R = R_0 \chi \mathbf{B} \cdot \mathbf{I}$ . This effect was heuristically derived by generalizing the Onsager's reciprocal theorem into the nonlinear regime (74).

Rikken *et al* once speculated the underlying connection between EMChA and CISS (20, 89). Our work reveals the unambiguous link between EMChA and the CISS-induced nonreciprocal MR (rather than the spin current). Both EMChA and the CISS-induced MR satisfy the global Onsager's reciprocity. The EMChA refers to the conductor regime where both the TRS- and IS-breaking occur. In comparison, the CISS-induced MR is induced by the IS-breaking in the conductor but the TRS-breaking in leads. By generalizing this symmetry condition in a two-terminal device, we can distribute the IS- and TRS-breaking to any of three regimes, including two leads and the conductor, to induce the nonreciprocity. We note that the magnetic leads can also be antiferromagnetic since some noncollinear antiferromagnets can also generate spin-polarized current (90). Also, the OPE provides one possible microscopic scenario for EMChA by revealing the role of the quantum orbital and SOC.

## Beyond the Chiral Structure

We point out that the OPE can also generate nontrivial spin-transport phenomena in non-helical and even non-chiral systems. The OPE is caused by orbital texture, which only requires the IS-breaking if TRS exists. The chiral structure represents a strong case of the inversion-breaking. If the induced orbital polarization may differ from the current direction, depending on the way of inversion-breaking.

Take an achiral chain for example, see **Figure 4a**. It is periodic along the  $z$  axis and has mirror reflection for  $x$ . The mirror symmetry forces orbitals  $L_z, L_y$  to vanish but allows the existence of  $L_x$ . In the band structure, the orbital texture refers to the locking between  $L_x$  and  $k_z$  (see Figure 4b). If leads are nonmagnetic, OPE induces nonzero  $G_{S_x}$  rather than  $G_{S_z}$  in the presence of SOC from the contact. If leads exhibit magnetization along the  $x$  direction, OPE induces the MR as reversing the magnetization. This model shows that the spin polarization does not necessarily align with the current flow. For a general noncentrosymmetric material (chiral or achiral), the orbital polarization depends on the specific symmetry. Therefore, we can engineer the geometric atomic structure to tailor the direction and magnitude of the spin-polarization.

The OPE-induced nonreciprocal MR in noncentrosymmetric systems coincides with the fact that EMChA was recently been generalized to ordinary IS-breaking materials for example, Si FET (91) and the polar semiconductor BiTeBr (92) and also predicted for noncentrosymmetric Weyl semimetals (93).

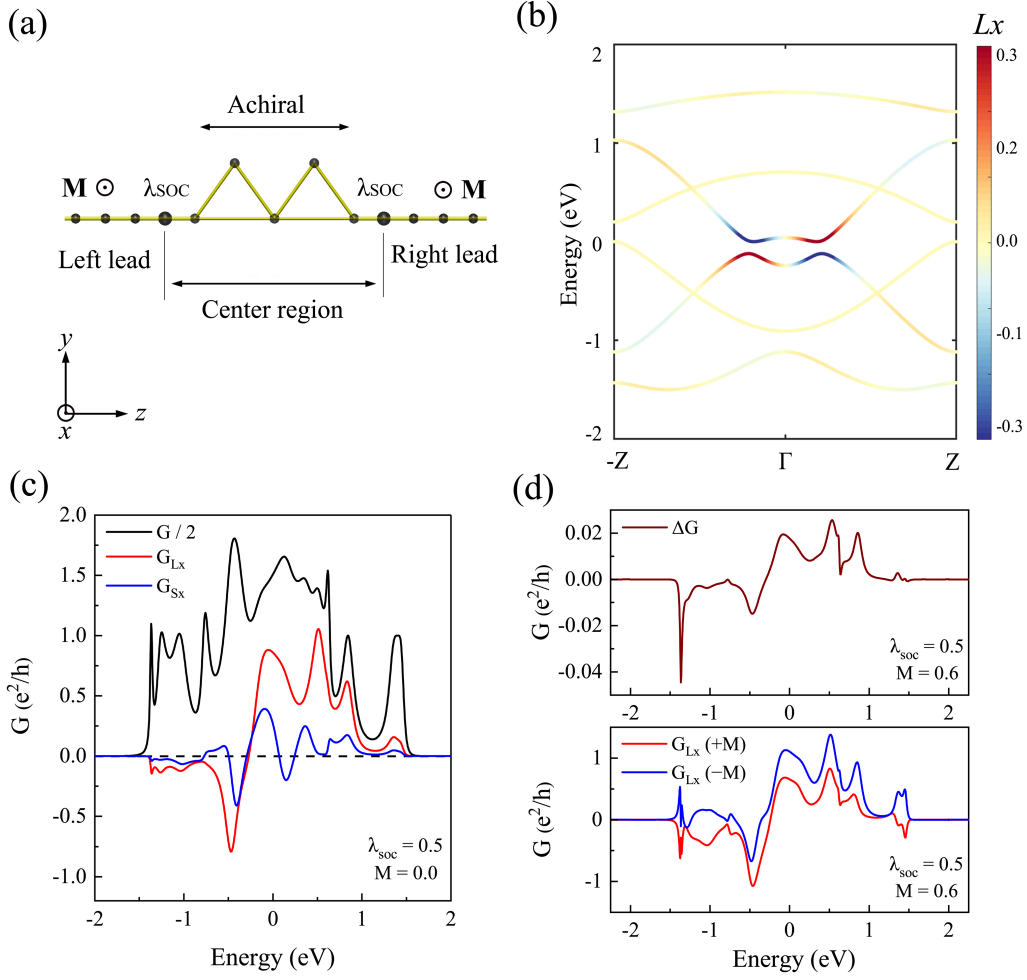


Figure 4: The orbital and spin polarization in an achiral system. (a) The device structure. The center region represents a molecule that has reflection symmetry but breaks inversion symmetry. (b) Corresponding band structure with  $L_x$  orbital polarization. (c) The conductance is both orbital and spin-polarized when leads are nonmagnetic. The spin-polarization is along the  $x$  direction rather than the  $z$  axis. (d) It also exhibits magnetoresistance (the dephasing  $\eta = 0.005$ ) as switching on the magnetization from the  $+x$  to  $-x$  directions in leads.

## Summary

In summary, our theory brings the missing block, the orbital degree of freedom, to understand the consequence of chiral atomic structures. The orbital polarization effect circumvents the weak SOC in organic molecules and explains the robustness of the CISS-induced phenomena, by the intense orbital texture in the molecule and the large SOC in the lead. The orbital texture provides an insightful quantity in the band structure to estimate the CISS effect for real materials. Additionally, our work resolves the debate on the dephasing. We found that the dephasing is unnecessary to generate the spin current when employing multi-channel leads while it is required to induce the MR and magnetic chiral selection. The nonreciprocal conductance can lead to current rectification and may be applied for photodetection or energy harvesting. From the OPE, we can deduce the EMChA independently, which refers to the nonreciprocal MR observed in the solid-state materials. Beyond helical molecules and even beyond the chiral structure, the OPE paves a way to manipulate the spin polarization by engineering the atomic structure in general noncentrosymmetric materials. Since the chirality is a common feature of many chemical and most biochemical systems, possibly the extent of OPE may be larger than one can imagine from the CISS, which calls for further investigations. Our work may provide a topological perspective to understand the fundamental role of chirality in the biological (94) and chemical (38, 95) systems.

## Methods

We calculate the band structure of  $3_{10}$  helix by the density-functional theory within the generalized gradient approximation (96) using the the Vienna Ab initio Simulation Package (VASP) (97). The orbital moment  $L_z$  is extracted from the phase-dependent atomic-orbital projection of the Bloch wave function. Information for the transport calculations can be found in the SM.

## Supplementary Materials

Supplementary material for this article is available at <http://XXX>.

Section S1. Tight-binding model of the helical chain.

Section S2 and Figure S1. Anisotropic hopping along the chiral chain

Section S3 and Figure S2. Model parameters for the transport calculations.

Figure S3. Band structures of the lead, the SOC region and the chiral molecule.

Figure S4. Verification of the global Onsager's reciprocal relation.

Figure S5. Orbital channel-specific conductance of the chiral chain.

Figure S6. Orbital channel-specific conductance of the achiral chain.

Figure S7. Influence of dephasing parameter  $\eta$  on spin conductance.

Figure S8. The orbital conserved lead and non-conserved lead in the achiral chain device.

## References and Notes

**Acknowledgements:** We thank gratefully the advice and help from Ady Stern and Yuval Oreg. We also acknowledge inspiring discussions with Ron Naaman, Yossi Paltiel, Zhong Wang, ChiYung Yam, Lukas Muechler, Tobias Holder, Raquel Queiroz, Karen Michaelia, Leeor Kronik, Shuichi Murakami, Eugene J. Mele and Claudia Felser. B.Y. honors the memory of Shoucheng Zhang who inspired him to study the chirality in both physics and biology. B.Y. acknowledges the financial support by the Willner Family Leadership Institute for the Weizmann Institute of Science, the Benozio Endowment Fund for the Advancement of Science, Ruth and Herman Albert Scholars Program for New Scientists, the European Research Council (ERC) under the European Union's Horizon 2020 research and innovation programme (Grant No. 815869).

**Competing Interests:** The authors declare that they have no competing interests.

**Data and materials availability:** All data needed to evaluate the conclusions in the paper are present in the paper and/or the Supplementary Materials. Additional data related to this paper may be requested from the authors.

\* Both authors contributed equally to this work.

† Email of correspondence: binghai.yan@weizmann.ac.il

## References

1. J. S. Siegel, Homochiral imperative of molecular evolution. *Chirality* **10**, 24–27 (1998).
2. L. Ma, C. Abney, W. Lin, Enantioselective catalysis with homochiral metal–organic frameworks. *Chemical Society Reviews* **38**, 1248–1256 (2009).
3. E. Francotte, W. Lindner, *Chirality in drug research*, vol. 33 (Wiley-VCH Weinheim, Weinheim, Germany, 2006).
4. H. Weyl, Gravitation and the electron. *Proceedings of the National Academy of Sciences of the United States of America* **15**, 323 (1929).
5. M. Goldhaber, L. Grodzins, A. W. Sunyar, Helicity of neutrinos. *Phys. Rev.* **109**, 1015–1017 (1958).
6. B. Gohler, V. Hamelbeck, T. Z. Markus, M. Kettner, G. F. Hanne, Z. Vager, R. Naaman, H. Zacharias, Spin Selectivity in Electron Transmission Through Self-Assembled Monolayers of Double-Stranded DNA. *Science* **331**, 894 – 897 (2011).
7. R. Naaman, D. H. Waldeck, Chiral-Induced Spin Selectivity Effect. *The Journal of Physical Chemistry Letters* **3**, 2178–2187 (2012).

8. R. Naaman, Y. Paltiel, D. H. Waldeck, Chiral molecules and the electron spin. *Nature Reviews Chemistry* **3**, 250–260 (2019).
9. K. Ray, S. P. Ananthavel, D. H. Waldeck, R. Naaman, Asymmetric Scattering of Polarized Electrons by Organized Organic Films of Chiral Molecules. *Science* **283**, 814–816 (1999).
10. I. Carmeli, V. Skakalova, R. Naaman, Z. Vager, Magnetization of Chiral Monolayers of Polypeptide: A Possible Source of Magnetism in Some Biological Membranes We are grateful to Prof. M. Fridkin and his group for helping us in the synthesis of the polyalanine. Partial support from the USIsrael Binational Science Foundation is acknowledged. *Angewandte Chemie International Edition* **41**, 761 (2002).
11. D. Mishra, T. Z. Markus, R. Naaman, M. Kettner, B. Ghler, H. Zacharias, N. Friedman, M. Sheves, C. Fontanesi, Spin-dependent electron transmission through bacteriorhodopsin embedded in purple membrane. *Proceedings of the National Academy of Sciences* **110**, 14872–14876 (2013).
12. M. Kettner, B. Goehler, H. Zacharias, D. Mishra, V. Kiran, R. Naaman, C. Fontanesi, D. H. Waldeck, S. Sek, J. Pawaowski, J. Juhaniewicz, Spin Filtering in Electron Transport Through Chiral Oligopeptides. *The Journal of Physical Chemistry C* **119**, 14542–14547 (2015).
13. T. J. Zwang, S. Hrlimann, M. G. Hill, J. K. Barton, Helix-Dependent Spin Filtering through the DNA Duplex. *Journal of the American Chemical Society* **138**, 15551–15554 (2016).
14. M. Kettner, V. V. Maslyuk, D. Nrenberg, J. Seibel, R. Gutierrez, G. Cuniberti, K.-H. Ernst, H. Zacharias, Chirality-Dependent Electron Spin Filtering by Molecular Monolayers of Helicenes. *The Journal of Physical Chemistry Letters* **9**, 2025–2030 (2018).
15. M. Eckshtain-Levi, E. Capua, S. Refaely-Abramson, S. Sarkar, Y. Gavrilov, S. P. Mathew, Y. Paltiel, Y. Levy, L. Kronik, R. Naaman, Cold denaturation induces inversion of dipole and spin transfer in chiral peptide monolayers. *Nature communications* **7**, 10744 (2016).
16. C. Kulkarni, A. K. Mondal, T. K. Das, G. Grinbom, F. Tassinari, M. F. J. Mabesoone, E. W. Meijer, R. Naaman, Highly Efficient and Tunable Filtering of Electrons' Spin by Supramolecular Chirality of Nanofiber-Based Materials. *Advanced Materials* **32**, 1904965 (2020).
17. F. Tassinari, J. Steidel, S. Paltiel, C. Fontanesi, M. Lahav, Y. Paltiel, R. Naaman, Enantioseparation by crystallization using magnetic substrates. *Chemical Science* **10**, 5246–5250 (2019).
18. H. Lu, J. Wang, C. Xiao, X. Pan, X. Chen, R. Brunecky, J. J. Berry, K. Zhu, M. C. Beard, Z. V. Vardeny, Spin-dependent charge transport through 2D chiral hybrid lead-iodide perovskites. *Science Advances* **5**, eaay0571 (2019).

19. A. Inui, R. Aoki, Y. Nishiue, K. Shiota, Y. Kousaka, H. Shishido, D. Hirobe, M. Suda, J.-i. Ohe, J.-i. Kishine, H. M. Yamamoto, Y. Togawa, Chirality-induced spin-polarized state of a chiral crystal  $\text{crnb}_3\text{S}_6$ . *Phys. Rev. Lett.* **124**, 166602 (2020).
20. G. L. J. A. Rikken, A New Twist on Spintronics. *Science* **331**, 864–865 (2011).
21. Z. Xie, Z. Xie, T. Z. Markus, S. R. Cohen, Z. Vager, R. Gutierrez, R. Naaman, Spin specific electron conduction through DNA oligomers. *Nano letters* **11**, 4652–5 (2011).
22. S. P. Mathew, P. C. Mondal, H. Moshe, Y. Mastai, R. Naaman, Non-magnetic organic/inorganic spin injector at room temperature. *Applied Physics Letters* **105**, 242408 (2014).
23. R. Naaman, D. H. Waldeck, Spintronics and Chirality: Spin Selectivity in Electron Transport Through Chiral Molecules. *Annual Review of Physical Chemistry* **66**, 263 – 281 (2015).
24. V. Kiran, S. P. Mathew, S. R. Cohen, I. H. Delgado, J. Lacour, R. Naaman, Helicenes-A New Class of Organic Spin Filter. *Advanced Materials* **28**, 1957–1962 (2016).
25. O. B. Dor, S. Yochelis, A. Radko, K. Vankayala, E. Capua, A. Capua, S.-H. Yang, L. T. Baczewski, S. S. P. Parkin, R. Naaman, Y. Paltiel, Magnetization switching in ferromagnets by adsorbed chiral molecules without current or external magnetic field. *Nature Communications* **8**, 14567 (2017).
26. H. Al-Bustami, G. Koplovitz, D. Primc, S. Yochelis, E. Capua, D. Porath, R. Naaman, Y. Paltiel, Single nanoparticle magnetic spin memristor. *Small* **14**, 1801249 (2018).
27. V. Varade, T. Markus, K. Vankayala, N. Friedman, M. Sheves, D. H. Waldeck, R. Naaman, Bacteriorhodopsin based non-magnetic spin filters for biomolecular spintronics. *Physical Chemistry Chemical Physics* **20**, 1091–1097 (2018).
28. E. Z. B. Smolinsky, A. Neubauer, A. Kumar, S. Yochelis, E. Capua, R. Carmieli, Y. Paltiel, R. Naaman, K. Michaeli, Electric Field-Controlled Magnetization in GaAs/AlGaAs Heterostructures Chiral Organic Molecules Hybrids. *The Journal of Physical Chemistry Letters* **10**, 1139–1145 (2019).
29. L. Jia, C. Wang, Y. Zhang, L. Yang, Y. Yan, Efficient Spin Selectivity in Self-Assembled Superhelical Conducting Polymer Microfibers. *ACS Nano* (2020).
30. S.-H. Yang, Spintronics on chiral objects. *Applied Physics Letters* **116**, 120502 (2020).
31. T. Liu, X. Wang, H. Wang, G. Shi, F. Gao, H. Feng, H. Deng, L. Hu, E. Lochner, P. Schlottmann, S. v. Molnr, Y. Li, J. Zhao, P. Xiong, Spin selectivity through chiral polyalanine monolayers on semiconductors. *arXiv 2001.00097* (2019).

32. W. Mtangi, V. Kiran, C. Fontanesi, R. Naaman, Role of the electron spin polarization in water splitting. *The journal of physical chemistry letters* **6**, 4916–4922 (2015).
33. W. Mtangi, F. Tassinari, K. Vankayala, A. Vargas Jentzsch, B. Adelizzi, A. R. Palmans, C. Fontanesi, E. Meijer, R. Naaman, Control of electrons spin eliminates hydrogen peroxide formation during water splitting. *Journal of the American Chemical Society* **139**, 2794–2798 (2017).
34. P. C. Mondal, W. Mtangi, C. Fontanesi, Chiro-Spintronics: Spin-Dependent Electrochemistry and Water Splitting Using Chiral Molecular Films. *Small Methods* **2**, 1700313 (2018).
35. F. Tassinari, K. Banerjee-Ghosh, F. Parenti, V. Kiran, A. Mucci, R. Naaman, Enhanced hydrogen production with chiral conductive polymer-based electrodes. *The Journal of Physical Chemistry C* **121**, 15777–15783 (2017).
36. K. B. Ghosh, W. Zhang, F. Tassinari, Y. Mastai, O. Lidor-Shalev, R. Naaman, P. Mllers, D. Nrenberg, H. Zacharias, J. Wei, E. Wierzbinski, D. H. Waldeck, Controlling Chemical Selectivity in Electrocatalysis with Chiral CuO-Coated Electrodes. *The Journal of Physical Chemistry C* **123**, 3024–3031 (2019).
37. K. Banerjee-Ghosh, O. B. Dor, F. Tassinari, E. Capua, S. Yochelis, A. Capua, S.-H. Yang, S. S. P. Parkin, S. Sarkar, L. Kronik, L. T. Baczewski, R. Naaman, Y. Paltiel, Separation of enantiomers by their enantiospecific interaction with achiral magnetic substrates. *Science* **360**, 1331–1334 (2018).
38. T. S. Metzger, S. Mishra, B. P. Bloom, N. Goren, A. Neubauer, G. Shmul, J. Wei, S. Yochelis, F. Tassinari, C. Fontanesi, D. H. Waldeck, Y. Paltiel, R. Naaman, The Electron Spin as a Chiral Reagent. *Angewandte Chemie International Edition* **59**, 1653–1658 (2020).
39. D. M. Stemer, J. M. Abendroth, K. M. Cheung, M. Ye, M. S. E. Hadri, E. E. Fullerton, P. S. Weiss, Differential Charging in Photoemission from Mercurated DNA Monolayers on Ferromagnetic Films. *Nano Letters* **20**, 1218–1225 (2020).
40. S. Ghosh, S. Mishra, E. Avigad, B. P. Bloom, L. T. Baczewski, S. Yochelis, Y. Paltiel, R. Naaman, D. H. Waldeck, Effect of Chiral Molecules on the Electrons' Spin Wavefunction at Interfaces. *The Journal of Physical Chemistry Letters* **11**, 1550–1557 (2020).
41. S. Yeganeh, M. A. Ratner, E. Medina, V. Mujica, Chiral electron transport: Scattering through helical potentials. *The Journal of Chemical Physics* **131**, 014707 (2009).
42. A.-M. Guo, Q.-f. Sun, Spin-Selective Transport of Electrons in DNA Double Helix. *Physical Review Letters* **108**, 218102 (2012).
43. A.-M. Guo, Q.-f. Sun, Sequence-dependent spin-selective tunneling along double-stranded DNA. *Physical Review B* **86**, 115441 (2012).

44. R. Gutierrez, E. Díaz, R. Naaman, G. Cuniberti, Spin-selective transport through helical molecular systems. *Phys. Rev. B* **85**, 081404 (2012).
45. R. Gutierrez, E. Diaz, C. Gaul, T. Brumme, F. Dominguez-Adame, G. Cuniberti, Modeling Spin Transport in Helical Fields: Derivation of an Effective Low-Dimensional Hamiltonian. *The Journal of Physical Chemistry C* **117**, 22276–22284 (2013).
46. J. Gersten, K. Kaasbjerg, A. Nitzan, Induced spin filtering in electron transmission through chiral molecular layers adsorbed on metals with strong spin-orbit coupling. *The Journal of Chemical Physics* **139**, 114111 (2013).
47. A.-M. Guo, E. Díaz, C. Gaul, R. Gutierrez, F. Domínguez-Adame, G. Cuniberti, Q.-f. Sun, Contact effects in spin transport along double-helical molecules. *Phys. Rev. B* **89**, 205434 (2014).
48. A.-M. Guo, Q.-F. Sun, Spin-dependent electron transport in protein-like single-helical molecules. *Proceedings of the National Academy of Sciences* **111**, 11658–11662 (2014).
49. E. Medina, L. A. Gonzalez-Arraga, D. Finkelstein-Shapiro, B. Berche, V. Mujica, Continuum model for chiral induced spin selectivity in helical molecules. *The Journal of Chemical Physics* **142**, 194308 (2015).
50. S. Matityahu, Y. Utsumi, A. Aharony, O. Entin-Wohlman, C. A. Balseiro, Spin-dependent transport through a chiral molecule in the presence of spin-orbit interaction and nonunitary effects. *Physical Review B* **93**, 075407 (2016).
51. S. Varela, V. Mujica, E. Medina, Effective spin-orbit couplings in an analytical tight-binding model of DNA: Spin filtering and chiral spin transport. *Physical Review B* **93**, 155436 (2016).
52. T.-R. Pan, A.-M. Guo, Q.-F. Sun, Spin-polarized electron transport through helicene molecular junctions. *Physical Review B* **94**, 235448 (2016).
53. K. Michaeli, V. Varade, R. Naaman, D. H. Waldeck, A new approach towards spintronics–spintronics with no magnets. *Journal of Physics: Condensed Matter* **29**, 103002 (2017).
54. S. Matityahu, A. Aharony, O. Entin-Wohlman, C. A. Balseiro, Spin filtering in all-electrical three-terminal interferometers. *Physical Review B* **95**, 085411 (2017).
55. V. V. Maslyuk, R. Gutierrez, A. Dianat, V. Mujica, G. Cuniberti, Enhanced Magnetoresistance in Chiral Molecular Junctions. *The Journal of Physical Chemistry Letters* **9**, 5453–5459 (2018).
56. E. Díaz, A. Contreras, J. Hernández, F. Domínguez-Adame, Effective nonlinear model for electron transport in deformable helical molecules. *Phys. Rev. E* **98**, 052221 (2018).

57. E. Díaz, F. Domínguez-Adame, R. Gutierrez, G. Cuniberti, V. Mujica, Thermal decoherence and disorder effects on chiral-induced spin selectivity. *The journal of physical chemistry letters* **9**, 5753–5758 (2018).
58. K. Michaeli, R. Naaman, Origin of Spin-Dependent Tunneling Through Chiral Molecules. *The Journal of Physical Chemistry C* **123**, 17043–17048 (2019).
59. D. Nuerenberg, H. Zacharias, Evaluation of spin-flip scattering in chirality-induced spin selectivity using the Riccati equation. *Physical Chemistry Chemical Physics* **21**, 3761–3770 (2019).
60. X. Yang, C. H. v. d. Wal, B. J. v. Wees, Spin-dependent electron transmission model for chiral molecules in mesoscopic devices. *Physical Review B* **99**, 024418 (2019).
61. S. Dalum, P. Hedegrd, Theory of Chiral Induced Spin Selectivity. *Nano Letters* **19**, 5253–5259 (2019).
62. X. Yang, C. H. v. d. Wal, B. J. v. Wees, Detecting chirality in two-terminal electronic devices. *arXiv 1912.09085* (2019).
63. X. Li, J. Nan, X. Pan, Chiral Induced Spin Selectivity as a Spontaneous Intertwined Order. *arXiv 2005.03656* (2020).
64. J. Fransson, Vibrational Origin of Exchange Splitting and Chirality Induced Spin Selectivity. *arXiv 2005.06753* (2020).
65. A. Ghazaryan, Y. Paltiel, M. Lemeshko, Analytic Model of Chiral-Induced Spin Selectivity. *The Journal of Physical Chemistry C* (2020).
66. S. Varela, I. Zambrano, B. Berche, V. Mujica, E. Medina, Spin-orbit interaction and spin selectivity for tunneling electron transfer in DNA. *arXiv 2003.00582* (2020).
67. J. D. Torres, R. Hidalgo, S. Varela, E. Medina, Mechanically modulated spin orbit couplings in oligopeptides. *arXiv 2005.08474* (2020).
68. A. Shitade, E. Minamitani, Geometric spin-orbit coupling and chirality-induced spin selectivity. *arXiv preprint arXiv:2002.05371* (2020).
69. Y. Utsumi, O. Entin-Wohlman, A. Aharony, Spin selectivity through time-reversal symmetric helical junctions. *arXiv 2005.04041* (2020).
70. F. Kuemmeth, S. Ilani, D. C. Ralph, P. L. McEuen, Coupling of spin and orbital motion of electrons in carbon nanotubes. *Nature* **452**, 448–452 (2008).
71. G. A. Steele, F. Pei, E. A. Laird, J. M. Jol, H. B. Meerwaldt, L. P. Kouwenhoven, Large spin-orbit coupling in carbon nanotubes. *Nature Communications* **4**, 1573 (2013).

72. B. Yan, C. Felser, Topological Materials: Weyl Semimetals. *Annu. Rev. Cond. Mat. Phys.* **8**, 337 – 354 (2017).
73. N. P. Armitage, E. J. Mele, A. Vishwanath, Weyl and Dirac semimetals in three-dimensional solids. *Rev. Mod. Phys.* **90**, 015001 (2018).
74. G. L. J. A. Rikken, J. Flling, P. Wyder, Electrical Magnetochiral Anisotropy. *Physical Review Letters* **87**, 236602 (2001).
75. F. Tassinari, D. R. Jayarathna, N. Kantor-Uriel, K. L. Davis, V. Varade, C. Achim, R. Naaman, Chirality Dependent Charge Transfer Rate in Oligopeptides. *Advanced Materials* **30**, 1706423 (2018).
76. S. A. Parameswaran, A. M. Turner, D. P. Arovas, A. Vishwanath, Topological order and absence of band insulators at integer filling in non-symmorphic crystals. *Nature Physics* **9**, 299 – 303 (2013).
77. S. M. Young, C. L. Kane, Dirac semimetals in two dimensions. *Phys. Rev. Lett.* **115**, 126803 (2015).
78. J. C. Slater, G. F. Koster, Simplified lcao method for the periodic potential problem. *Phys. Rev.* **94**, 1498–1524 (1954).
79. M. Büttiker, Four-terminal phase-coherent conductance. *Phys. Rev. Lett.* **57**, 1761–1764 (1986).
80. C. W. Groth, M. Wimmer, A. R. Akhmerov, X. Waintal, Kwant: a software package for quantum transport. *New Journal of Physics* **16**, 063065 (2014).
81. A. A. Kiselev, K. W. Kim, Prohibition of equilibrium spin currents in multiterminal ballistic devices. *Physical Review B* **71**, 153315 (2005).
82. J. H. Bardarson, A proof of the Kramers degeneracy of transmission eigenvalues from antisymmetry of the scattering matrix. *Journal of Physics A: Mathematical and Theoretical* **41**, 405203 (2008).
83. M. Bttiker, Role of quantum coherence in series resistors. *Physical Review B* **33**, 3020–3026 (1986).
84. S. Mishra, A. K. Mondal, S. Pal, T. K. Das, E. Z. B. Smolinsky, G. Siligardi, R. Naaman, Length-Dependent Electron Spin Polarization in Oligopeptides and DNA. *The Journal of Physical Chemistry C* **124**, 10776–10782 (2020).
85. M. Büttiker, Symmetry of electrical conduction. *IBM Journal of Research and Development* **32**, 317–334 (1988).

86. R. Naaman, D. H. Waldeck, Comment on “Spin-dependent electron transmission model for chiral molecules in mesoscopic devices”. *Physical Review B* **101**, 026403 (2020).
87. X. Yang, C. H. van der Wal, B. J. van Wees, Reply to “comment on ‘spin-dependent electron transmission model for chiral molecules in mesoscopic devices’”. *Phys. Rev. B* **101**, 026404 (2020).
88. Y. Tokura, N. Nagaosa, Nonreciprocal responses from non-centrosymmetric quantum materials. *Nature Communications* **9**, 3740 (2018).
89. G. L. J. A. Rikken, N. Avarvari, Strong electrical magnetochiral anisotropy in tellurium. *Phys. Rev. B* **99**, 245153 (2019).
90. J. Zelezny, Y. Zhang, C. Felser, B. Yan, Spin-Polarized Current in Noncollinear Antiferromagnets. *Physical review letters* **119**, 187204 (2017).
91. G. L. J. A. Rikken, P. Wyder, Magnetoelectric Anisotropy in Diffusive Transport. *Physical Review Letters* **94**, 016601 (2005).
92. T. Ideue, K. Hamamoto, S. Koshikawa, M. Ezawa, S. Shimizu, Y. Kaneko, Y. Tokura, N. Nagaosa, Y. Iwasa, Bulk rectification effect in a polar semiconductor. *Nature Physics* **13**, 578–583 (2017).
93. T. Morimoto, N. Nagaosa, Chiral Anomaly and Giant Magnetochiral Anisotropy in Noncentrosymmetric Weyl Semimetals. *Physical Review Letters* **117**, 146603 (2016).
94. A. Kumar, E. Capua, M. K. Kesharwani, J. M. L. Martin, E. Sitbon, D. H. Waldeck, R. Naaman, Chirality-induced spin polarization places symmetry constraints on biomolecular interactions. *Proceedings of the National Academy of Sciences* **114**, 2474–2478 (2017).
95. M. Innocenti, M. Passaponti, W. Giurlani, A. Giacomino, L. Pasquali, R. Giovanardi, C. Fontanesi, Spin dependent electrochemistry: Focus on chiral vs achiral charge transmission through 2D SAMs adsorbed on gold. *Journal of Electroanalytical Chemistry* **856**, 113705 (2020).
96. J. P. Perdew, K. Burke, M. Ernzerhof, Generalized gradient approximation made simple. *Physical Review Letters* **77**, 3865 (1996).
97. G. Kresse, J. Furthmüller, Efficient iterative schemes for ab initio total-energy calculations using a plane-wave basis set. *Physical Review B* **54**, 11169 (1996).

# Supplementary Materials for “Chirality Induced Quantum Orbital Polarization Effect in Chiral Molecules”

Yizhou Liu\*, Jiewen Xiao\*, Jahyun Koo, Binghai Yan†

Department of Condensed Matter Physics, Weizmann Institute of Science, Rehovot 76100, Israel

## S1. TIGHT-BINDING MODEL

For the helix model with the three-fold skew rotation, there are three atomic sites ( $R \cos(i-1)2\pi/3, R \sin(i-1)2\pi/3, z_0(i-1)$  ( $i = 1, 2, 3$ )) within the unit cell, where  $i$  is the site number. We set the orbital bases  $p_x, p_y, p_z$  on each site. The onsite energy of  $p$  orbitals are set to zero while the nearest neighboring hopping is modelled by the Slater-Koster hopping. Therefore, the spinless Hamiltonian  $H(k_z)$  can be expressed in the  $p_{x,y,z}$  orbitals of three atomic sites,

$$H(k_z) = \begin{pmatrix} 0 & T_{12} \exp(-ik_z \cdot a/3) & T_{13} \exp(+ik_z \cdot a/3) \\ T_{21} \exp(+ik_z \cdot a/3) & 0 & T_{23} \exp(-ik_z \cdot a/3) \\ T_{31} \exp(-ik_z \cdot a/3) & T_{32} \exp(+ik_z \cdot a/3) & 0 \end{pmatrix}, \quad (\text{S1})$$

where 1, 2, 3 represent the atomic sites in the unitcell,  $k_z$  and  $a$  are the wave vector and lattice constant in the  $z$  direction, respectively.  $T_{ij}$  is the nearest-neighbor hopping matrix from site  $i$  to site  $j$  and can be written as

$$T_{ij}(\phi_{ij}, \theta_{ij}) = \begin{pmatrix} t_{ij,xx} & t_{ij,xy} & t_{ij,xz} \\ t_{ij,yx} & t_{ij,yy} & t_{ij,yz} \\ t_{ij,zx} & t_{ij,zy} & t_{ij,zz} \end{pmatrix} \quad (\text{S2})$$

$$\begin{aligned} t_{ij,xx} &= t_\pi \sin^2 \phi_{ij} + \cos^2 \phi_{ij} (t_\sigma \sin^2 \theta_{ij} + t_\pi \cos^2 \theta_{ij}) \\ t_{ij,yy} &= t_\pi \cos^2 \phi_{ij} + \sin^2 \phi_{ij} (t_\sigma \sin^2 \theta_{ij} + t_\pi \cos^2 \theta_{ij}) \\ t_{ij,zz} &= t_\sigma \cos^2 \theta_{ij} + t_\pi \sin^2 \theta_{ij} \\ t_{ij,xy} &= t_{ij,yx} = \sin \phi_{ij} \cos \phi_{ij} (t_\sigma \sin^2 \theta_{ij} - t_\pi \cos^2 \theta_{ij}) \\ t_{ij,xz} &= t_{ij,zx} = \cos \phi_{ij} \sin \theta_{ij} \cos \theta_{ij} (t_\sigma - t_\pi) \\ t_{ij,yz} &= t_{ij,zy} = \sin \phi_{ij} \sin \theta_{ij} \cos \theta_{ij} (t_\sigma - t_\pi) \end{aligned} \quad (\text{S3})$$

Here,  $\phi_{ij}$  and  $\theta_{ij}$  are the spherical coordinates of site  $j$  relative to site  $i$ . For the helix molecule,  $\theta_{ij}$  is set to  $\pm\pi/4$  (so that  $z_0 = 2\sqrt{3}R$ ), and  $\phi_{ij}$  can adopt  $\pm\pi/6, \pm5\pi/6, \pm3\pi/2$  value. For the hopping parameter,  $t_\sigma$  and  $t_\pi$  are 1.5 eV and -0.5 eV respectively. With the above parameter, band structure is calculated and shown in Figure 1(b).

## S2. ANISOTROPIC HOPPING ALONG THE CHIRAL CHAIN

In the last section, we derive the hopping matrix from site  $i$  to site  $j$  under  $p_x, p_y, p_z$  bases. To understand the chiral selection from the anisotropic hopping, we write  $T_{ij}$  under the  $p_+, p_0, p_-$  orbital basis,

$$T_{ij}(\phi_{ij}, \theta_{ij}) = \begin{pmatrix} t_{ij,++} & t_{ij,+0} & t_{ij,+ -} \\ t_{ij,0+} & t_{ij,00} & t_{ij,0-} \\ t_{ij,-+} & t_{ij,-0} & t_{ij,- -} \end{pmatrix} \quad (\text{S4})$$

$$\begin{aligned}
t_{ij,++} &= (t_\pi(1 + \cos^2 \theta_{ij}) + t_\sigma \sin^2 \theta_{ij})/2 \\
t_{ij,00} &= t_\sigma \cos^2 \theta_{ij} + t_\pi \sin^2 \theta_{ij} \\
t_{ij,--} &= (t_\pi(1 + \cos^2 \theta_{ij}) + t_\sigma \sin^2 \theta_{ij})/2 \\
t_{ij,+0} &= t_{ij,0-} = ((t_\sigma - t_\pi) \sin \theta_{ij} \cos \theta_{ij} \exp(-i\phi_{ij}))/\sqrt{2} \\
t_{ij0,+} &= t_{ij,-0} = ((t_\sigma - t_\pi) \sin \theta_{ij} \cos \theta_{ij} \exp(+i\phi_{ij}))/\sqrt{2} \\
t_{ij,+-} &= ((t_\sigma - t_\pi) \sin^2 \theta_{ij} \exp(-i2\phi_{ij}))/2 \\
t_{ij,-+} &= ((t_\sigma - t_\pi) \sin^2 \theta_{ij} \exp(+i2\phi_{ij}))/2
\end{aligned} \tag{S5}$$

For the right-hand helical chain with the  $n$ -fold screw rotation, Figure S1 shows the electron hopping from site  $i$  to adjacent site  $i - 1$  and site  $i + 1$ , and such process can be denoted as 'd' (down) and 'u' (up) respectively. Therefore, the hopping matrix is written as  $T_d = T_{i(i-1)}(\pi - \phi/2, -\theta)$  and  $T_u = T_{i(i+1)}(\phi/2, \theta)$ , and their relation can be further derived:

$$\begin{aligned}
T_u &= \begin{pmatrix} t_{u++} & t_{u+0} & t_{u+-} \\ t_{u0+} & t_{u00} & t_{u0-} \\ t_{u-+} & t_{u-0} & t_{u--} \end{pmatrix} \\
&= \begin{pmatrix} t_{d++} \cdot e^{-i2\pi \cdot \Delta L_{z++}/n} & t_{d+0} \cdot e^{-i2\pi \cdot \Delta L_{z+0}/n} & t_{d+-} \cdot e^{-i2\pi \cdot \Delta L_{z+-}/n} \\ t_{d0+} \cdot e^{-i2\pi \cdot \Delta L_{z0+}/n} & t_{d00} \cdot e^{-i2\pi \cdot \Delta L_{z00}/n} & t_{d0-} \cdot e^{-i2\pi \cdot \Delta L_{z0-}/n} \\ t_{d-+} \cdot e^{-i2\pi \cdot \Delta L_{z-+}/n} & t_{d-0} \cdot e^{-i2\pi \cdot \Delta L_{z-0}/n} & t_{d--} \cdot e^{-i2\pi \cdot \Delta L_{z--}/n} \end{pmatrix}
\end{aligned} \tag{S6}$$

Therefore, suppose there are two orbitals  $p$  and  $q$ , the phase factor that connects the hopping term  $t_{upq}$  and  $t_{dpq}$  can be expressed as  $e^{-i2\pi \cdot \Delta L_{zpq}/n}$ , where  $\Delta L_{zpq}$  is the  $z$ -component angular momentum ( $L_z$ ) differences between orbital  $p$  and orbital  $q$ . For the intra-orbital and inter-orbital hopping, we further have:

$$t_{u++} = t_{u--} = t_{d++} = t_{d--} \tag{S7}$$

$$t_{u00} = t_{d00} \tag{S8}$$

$$t_{u+-} = t_{d+-} e^{-i4\pi/n} \tag{S9}$$

$$t_{u+0} = t_{u0-} = t_{d+0} e^{-i2\pi/n} = t_{d0-} e^{-i2\pi/n} \tag{S10}$$

To validate the above  $T_u$  and  $T_d$  relation expressed by the differences of angular momentum, we further consider the  $d$ -orbital hopping in the chiral chain, with  $L_z = 2, 1, 0, -1, -2$ . Similarly, the hopping matrix from site  $i$  to site  $j$  under the  $d_{2i}, d_{1i}, d_{0i}, d_{-1i}, d_{-2i}$  orbital basis can be written as:

$$T_{ij}(\phi_{ij}, \theta_{ij}) = \begin{pmatrix} t_{ij-2-2} & t_{ij-2-1} & t_{ij-20} & t_{ij-21} & t_{ij-22} \\ t_{ij-1-2} & t_{ij-1-1} & t_{ij-10} & t_{ij-11} & t_{ij-12} \\ t_{ij0-2} & t_{ij0-1} & t_{ij00} & t_{ij01} & t_{ij02} \\ t_{ij1-2} & t_{ij1-1} & t_{ij10} & t_{ij11} & t_{ij12} \\ t_{ij2-2} & t_{ij2-1} & t_{ij20} & t_{ij21} & t_{ij22} \end{pmatrix} \tag{S11}$$

$$\begin{aligned}
t_{ij22} &= t_{ij-2-2} = (3t_\sigma - 4t_\pi + t_\delta) \sin^4 \theta / 8 + t_\pi \sin^2 \theta + t_\delta \cos^2 \theta \\
t_{ij11} &= t_{ij-1-1} = (3t_\sigma - 4t_\pi + t_\delta) \sin^2 \theta \cos^2 \theta / 2 + t_\pi (1 + \cos^2 \theta) + t_\delta \sin^2 \theta \\
t_{ij00} &= t_\sigma (\sin^2 \theta - \cos^2 \theta)^2 / 4 + 3t_\pi \sin^2 \theta \cos^2 \theta + 3t_\delta \sin^4 \theta / 4
\end{aligned} \tag{S12}$$

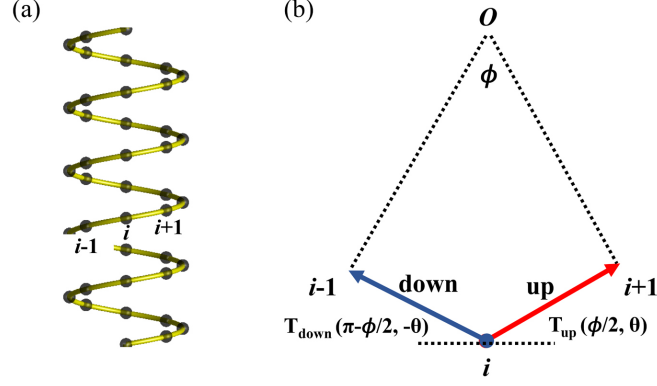


FIG. S1. Anisotropic hopping in the chiral chain. For the right hand helical chain, the hopping process from site  $i$  to  $i - 1$  and from site  $i$  to site  $i + 1$  can be denoted as 'd' (down) and 'u' (up), respectively.

$$\begin{aligned}
t_{ij21} &= t_{ij12}^\dagger = -t_{ij-1-2} = -t_{ij-2-1}^\dagger \\
&= (4(t_\delta - t_\pi) \sin 2\theta - (3t_\sigma - 4t_\pi + t_\delta) \sin^2 \theta \sin 2\theta) e^{-i\phi} \\
t_{ij20} &= t_{ij02}^\dagger = t_{ij0-2} = t_{ij-20}^\dagger \\
&= (\sqrt{6} \sin^2 \theta / 8) (t_\sigma (\cos^2 \theta - \sin^2 \theta) - 4t_\pi \cos^2 \theta + t_\delta (1 + \cos^2 \theta)) e^{-i2\phi} \\
t_{ij2-1} &= t_{ij-12}^\dagger = -t_{ij1-2} = -t_{ij-21}^\dagger \\
&= (\sin 2\theta \sin^2 \theta / 8) (3t_\sigma - 4t_\pi + t_\delta) e^{-i3\phi} \\
t_{ij2-2} &= t_{ij-22}^\dagger \\
&= (\sin^4 \theta / 8) (3t_\sigma - 4t_\pi + t_\delta) e^{-i4\phi} \\
t_{ij10} &= t_{ij01}^\dagger = -t_{ij0-1} = -t_{ij-10}^\dagger \\
&= (\sqrt{3} \sin \theta \cos \theta / 4) (t_\sigma (2 \cos^2 \theta - \sin^2 \theta) - 2t_\pi \cos 2\theta + t_\delta \sin^2 \theta) e^{-i\phi} \\
t_{ij1-1} &= t_{ij-11}^\dagger \\
&= (\sin^2 \theta / 2) ((t_\delta - t_\pi) - (3t_\sigma - 4t_\pi + t_\delta) \cos^2 \theta) e^{-i2\phi}
\end{aligned} \tag{S13}$$

With  $T_d = T_{i(i-1)}(\pi - \phi/2, -\theta)$  and  $T_u = T_{i(i+1)}(\phi/2, \theta)$ , the general relation between the matrix element  $t_{upq}$  in  $T_u$  and  $t_{dpq}$  in  $T_d$  can be written as (where  $p$  and  $q$  are  $d$  orbitals, and  $\Delta L_{zpq}$  is the  $L_z$  difference between them):

$$t_{upq} = t_{dpq} \exp(-i2\pi \cdot \Delta L_{zpq} / n) \tag{S14}$$

### S3. MODEL PARAMETERS FOR THE TRANSPORT CALCULATIONS

Hopping parameters for the two terminal device are presented in Figure S2, and their values are specified in the attached codes. To calculate the orbital channel-specific conductance of the achiral chain, we set the isotropic hopping  $t$  in leads. We also test the spin channel-specific conductance for both the isotropic hopping ( $t = t_\sigma = t_\pi = 1.3$  eV, orbital  $L_x$  conserved) and the general anisotropic hopping ( $t_\sigma = 1.5$  eV,  $t_\pi = 1.3$  eV, orbital  $L_x$  non-conserved) in leads, and results in Figure S6 display the similar feature.

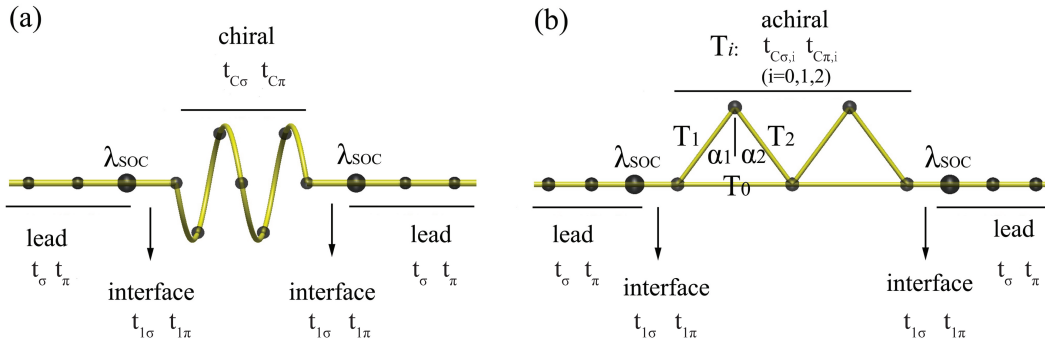


FIG. S2. Hopping parameters for the two-terminal device: (a) chiral molecule, and (b) achiral molecule.

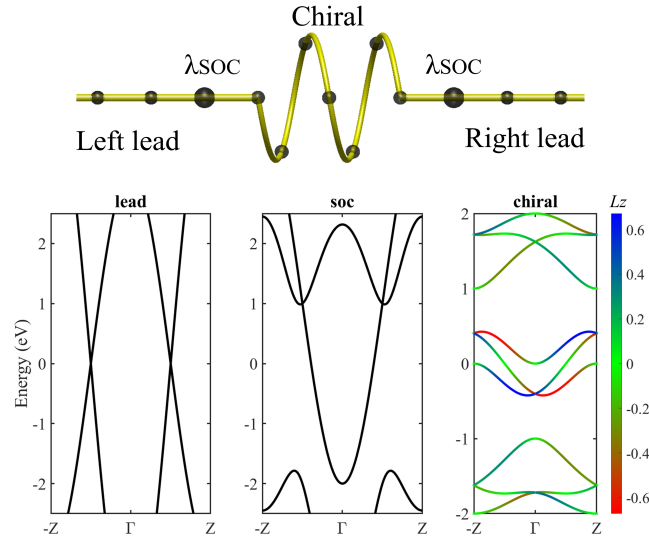


FIG. S3. Band structures of the lead, the SOC region and the chiral molecule. The chiral molecule is represented by the right-hand helix model discussed above and related hopping parameters and SOC strength are detailed in the section S3.

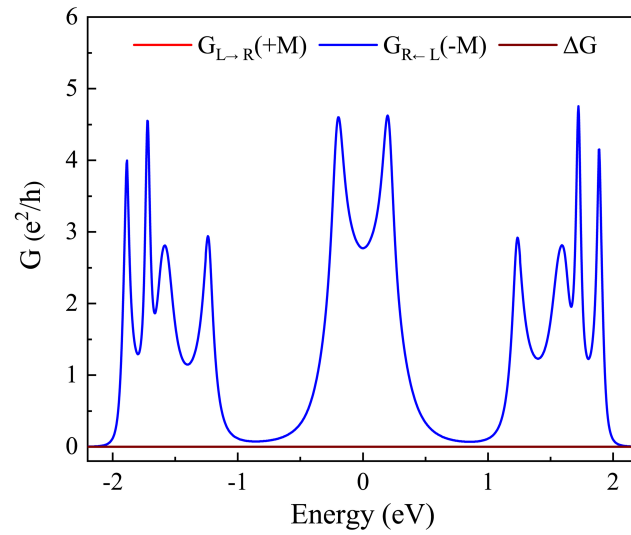


FIG. S4. Verification of the global Onsager's reciprocal relation. When dephasing term  $\eta$  is set to zero,  $\Delta G = G_{L \rightarrow R}(M) - G_{R \rightarrow L}(-M) = 0$ .

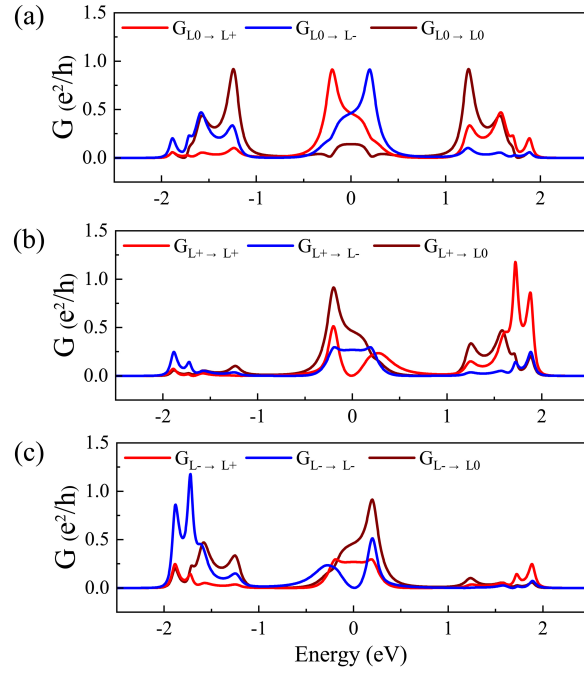


FIG. S5. Orbital channel-specific conductance of the chiral chain. Nine kinds of conductance from  $L_+, L_0, L_-$  orbital channel in the left lead to the  $L_+, L_0, L_-$  orbital channel in the right lead are presented (SOC strength is set to zero.)

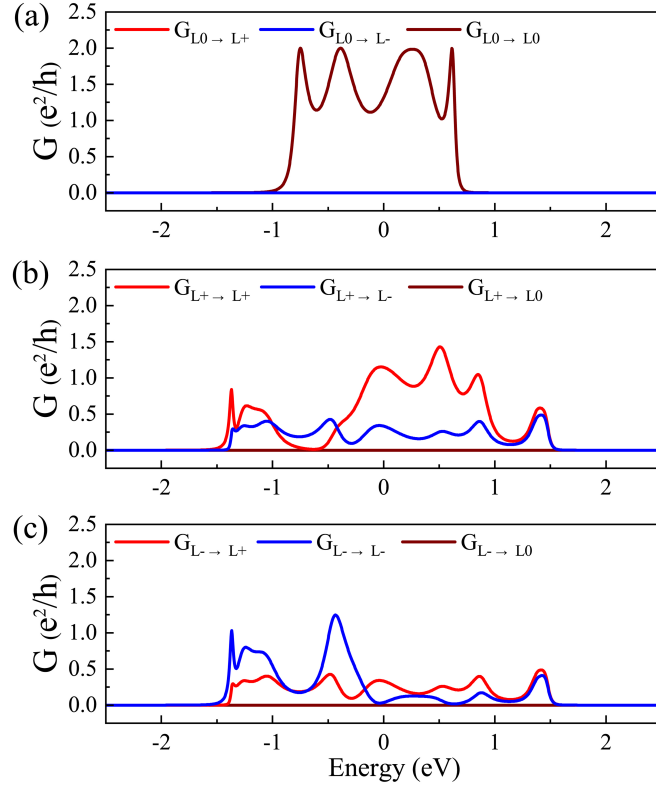


FIG. S6. Orbital channel-specific conductance for the achiral chain. Nine kinds of conductance from  $L_+, L_0, L_-$  orbital channel in the left lead to the  $L_+, L_0, L_-$  orbital channel in the right lead are presented (SOC strength is set to zero.)

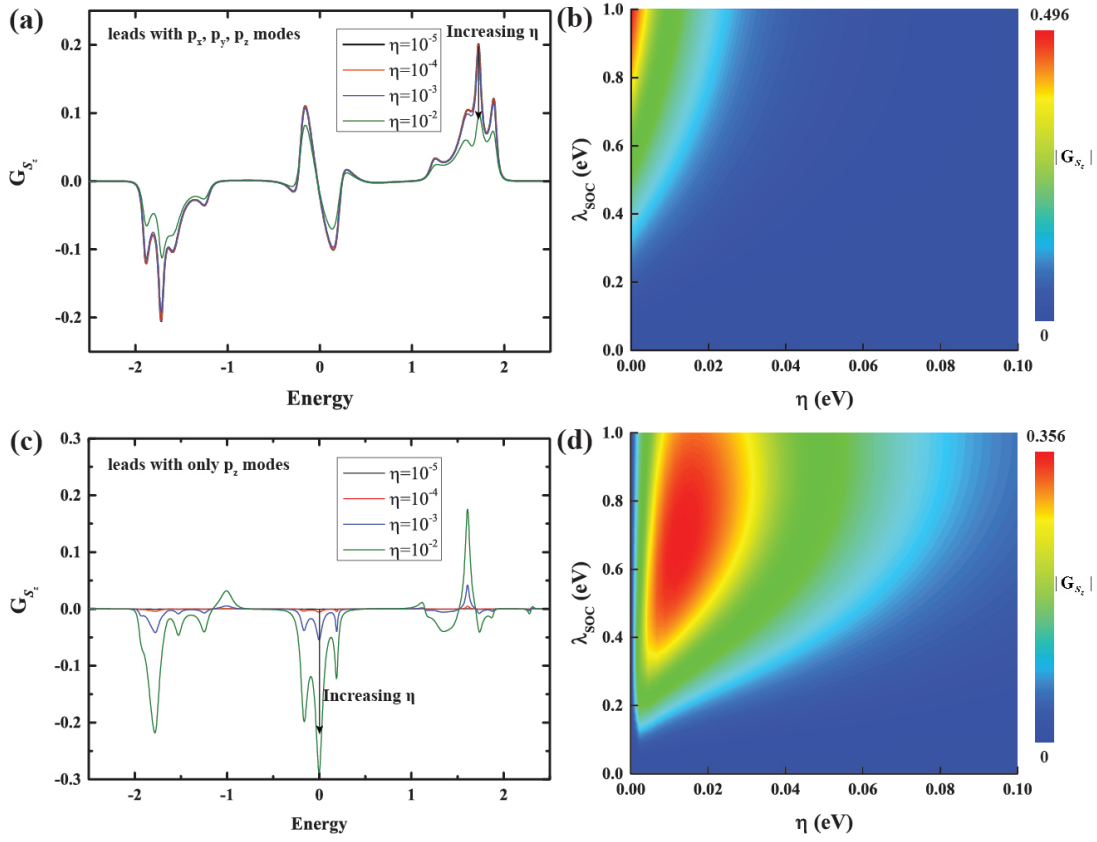


FIG. S7. Influence of dephasing parameter  $\eta$  on spin conductance  $G_{S_z}$  of (a)-(b) multiple-mode leads and (c)-(d) single-mode leads, respectively. (a), (c)  $G_{S_z}$  as function of energy for various  $\eta$ . (b), (d)  $G_{S_z}$  as function of  $\eta$  and  $\lambda_{\text{SOC}}$  at fixed energy (indicated by the arrows in (a) and (c), respectively). The single-mode leads are created by setting  $t_{\pi}^{\text{leads}} = 0$  so that only  $p_z$  modes (with two spins) contribute to spin and charge transport. For single-mode leads a finite dephasing is needed to generate nonzero  $G_{S_z}$  whereas for multiple-mode leads it is not necessary.

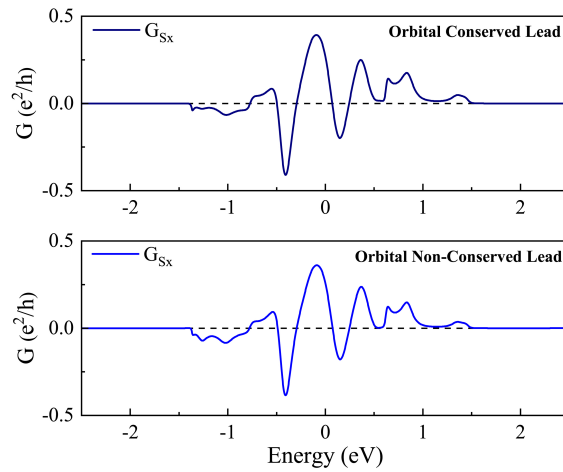


FIG. S8. Spin conductance  $G_{S_x}$  for the  $L_x$  orbital conserved lead and non-conserved lead in the achiral chain device. Detailed hopping parameters are shown in section S3.